Magnetic properties of RFe$_2$Zn$_{20}$ and RCo$_2$Zn$_{20}$ (R=Y, Nd, Sm, Gd–Lu)

Shuang Jia (贾爽),* Ni Ni (倪霓), S. L. Bud'ko, and P. C. Canfield
Ames Laboratory and Department of Physics and Astronomy, Iowa State University, Ames, Iowa 50011, USA
(Received 9 April 2009; revised manuscript received 29 July 2009; published 4 September 2009)

Magnetization, resistivity, and specific heat measurements were performed on solution-grown single crystals of RFe$_2$Zn$_{20}$ and RCo$_2$Zn$_{20}$ (R=Y,Nd,Sm,Gd-Lu). Whereas LuCo$_2$Zn$_{20}$ and YCo$_2$Zn$_{20}$ manifest unremarkable metallic behavior, LuFe$_2$Zn$_{20}$ and YFe$_2$Zn$_{20}$ display behaviors such as characteristic of nearly ferromagnetic Fermi liquids. When the well-defined 4f local moments (Gd^{3+}-Tm^{3+}) are embedded into this strongly polarizable host, they manifest enhanced ferromagnetic ordering and the values of T_C for RFe$_2$Zn$_{20}$ (R=Gd-Tm) scale with the de Gennes factor. In addition, data on the RFe$_2$Zn$_{20}$ compounds indicate a small crystal electric field (CEF) effect compared with the interaction energy scale. On the other hand, the local moment bearing members of RCo$_2$Zn$_{20}$ (R=Nd,Sm,Gd-Tm) manifest weak magnetic interactions and the magnetic properties for R=Dy-Tm members are strongly influenced by the CEF effect on the R ions. The magnetic anisotropy and specific heat data for the Co series were used to determine the CEF coefficient of R ion with its cubic point symmetry. These CEF coefficients, determined for the Co series, are consistent with the magnetic anisotropy and specific heat data for the Fe series, which indicates similar CEF effects for the Fe and Co series. Such analysis, combined with specific heat and resistivity data, indicates that for R=Tb-Ho, the CEF splitting scale is smaller than their T_C values, whereas for ErFe$_2$Zn$_{20}$ and TmFe$_2$Zn$_{20}$ the 4f electrons lose part of their full Hund's rule ground state degeneracy above T_C. YbFe$_2$Zn$_{20}$ and YbCo$_2$Zn$_{20}$ manifest typical but distinct heavy fermion behaviors associated with different Kondo temperatures.

DOI: 10.1103/PhysRevB.80.104403 PACS number(s): 75.30.Gw, 75.50.Ee, 75.50.Cc

I. INTRODUCTION

Intermetallic compounds consisting of rare-earth and transition metals, as well as metalloids, have versatile magnetic properties.[1,2] Compounds with itinerant d electrons are of particular interest when they are in the vicinity of the Stoner transition: such systems, characterized as nearly or weakly ferromagnet, display strongly correlated electronic properties.[3] On the other hand, heavy rare-earth ions manifest magnetic versatility associated with the 4f electrons: null magnetism (Y^{3+} or Lu^{3+}), pure spin, local moment magnetism (Gd^{3+}), potentially anisotropic, crystal electric field (CEF) splitting, local moment magnetism (Tb^{3+}-Tm^{3+}), and more exotic magnetism; Yb ions may hybridize with conduction electrons and manifest so-called heavy fermion behavior. Series of compounds that combine these interesting properties has long attracted the attention of physicists. For example, the binary RCo$_2$ (R=rare earth) compounds, with the nearly ferromagnetic (FM) end members YCo$_2$ and LuCo$_2$, and the local moment FM members (R=Pr,Nd,Gd-Tm) have been studied for more than 35 years.[4,5]

Discovered by Nasch *et al.*,[6] the RT_2Zn$_{20}$ (R=rare earth, T=transition metal in the Fe, Co, and Ni groups) series of compounds crystallizes in the cubic CeCr$_2$Al$_{20}$ structure.[7–9] The R and T ions occupy their own single, unique, crystallographic sites with cubic and trigonal point symmetries, respectively, whereas the Zn ions have three unique crystallographic sites [Fig. 1(a)]. Both the R and the T ions are fully surrounded by shells of Zn that consist of the nearest neighbors (NNs) and the next nearest neighbors (NNNs). This means that there are no R-R, T-T, or R-T nearest neighbor and the shortest R-R spacing is ~6 Å. For the R ions, a Frank-Kasper polyhedron with coordinate number (CN) 16 is formed from 4 Zn NNs on the 16c site and 12 Zn NNNs on the 96g site [Fig. 1(b)].

Recently, studies of the thermodynamic and transport properties of these intermetallics have revealed varied magnetic behavior.[10–13] YFe$_2$Zn$_{20}$ and LuFe$_2$Zn$_{20}$ are archetypical examples of nearly ferromagnetic Fermi liquids (NFFLs) with Stoner enhancement factors of Z=0.88 [where $\chi_{T=0}=\chi_{Pauli}/(1-Z)$]. By embedding large Heisenberg-type moments associated with Gd^{3+} ions in this highly polarizable medium, GdFe$_2$Zn$_{20}$ manifests highly enhanced FM order. On the other hand, GdCo$_2$Zn$_{20}$ manifests ordinary, low temperature, antiferromagnetic (AFM) order, correspondent to the "normal metal" behavior of the conduction electron host, YCo$_2$Zn$_{20}$.[10] In addition to these interesting 3d electron and local moment properties, six related YbT_2Zn$_{20}$ compounds (T=Fe, Co, Ru, Rh, Os, and Ir) show heavy fermion ground states associated with different Kondo temperatures (T_K) and Yb ion degeneracies.[11]

Given the similarities and differences between the RFe$_2$Zn$_{20}$ and RCo$_2$Zn$_{20}$ (R=Gd,Y,Lu) series, it becomes important to study all of the R=Y,Gd-Lu members in detail. A comparative study of the RFe$_2$Zn$_{20}$ and RCo$_2$Zn$_{20}$ series

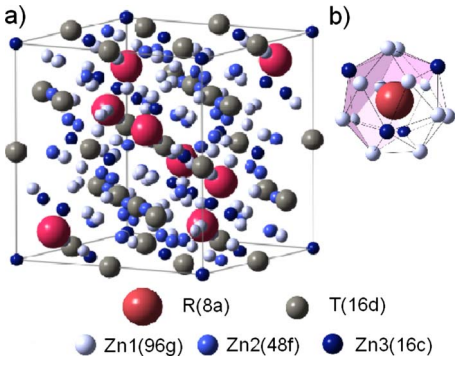

FIG. 1. (Color online) (a) The cubic unit cell of RT_2Zn$_{20}$. (b) The CN-16 Frank-Kasper polyhedron of rare-earth ions.

will help us to further understand the magnetic interaction between the local moments by means of the strongly polarizable medium, particularly with the CEF effect associated with nonzero orbital angular momentum. Furthermore, given the virtually identical CN-16 Frank-Kasper polyhedron for R ions, as well as the less than 2% difference of lattice constants for the whole RT_2Zn_{20} families, the study of the CEF effect on these local moment members will also help in the understanding of the varied heavy fermion states of YbT_2Zn_{20}, which were thought to be due to the competition between temperature scales associated with the CEF splitting and the Kondo effect.[11]

In this paper, we present the results of magnetization, heat capacity, and resistivity measurements on RFe_2Zn_{20} and RCo_2Zn_{20} (R=Y, Nd, Sm, Gd-Lu) compounds. Compared with the weakly correlated behaviors for YCo_2Zn_{20} and $LuCo_2Zn_{20}$, YFe_2Zn_{20} and $LuFe_2Zn_{20}$ manifest clear NFFL behaviors associated with the spin fluctuation of the itinerant electrons. For the RFe_2Zn_{20} compounds (R=Gd-Tm), the well-defined local moment members all manifest enhanced FM ordering with T_C values that roughly scale with the de Gennes factor. Their anomalous temperature-dependent susceptibility and resistivity can be explained as the result of local moments embedded in a NFFL host. In contrast, for the RCo_2Zn_{20} series, only Gd and Tb members manifest AFM ordering above 2 K, and the magnetic properties for R =Dy-Tm clearly manifest features associated with single-ion CEF effects associated with the R ions in a coordination of cubic symmetry. For the R=Tb-Tm members in the Co series, the CEF parameters can be determined from the magnetic anisotropy and the specific heat data and are roughly consistent with the results of calculations using a point charge model. For the Fe series, the R=Tb-Tm members show moderate magnetic anisotropy in their ordered states mainly due to the CEF effect on the R ions, which is consistent with the magnetic anisotropy found for the Co members. These results, as well as the analysis of the heat capacity and resistivity data, indicate that the FM state emerges from the fully degenerate Hund's rule ground state for RFe_2Zn_{20} (R =Gd-Ho), whereas $ErFe_2Zn_{20}$ and $TmFe_2Zn_{20}$ manifest CEF splitting above their Curie temperatures.

II. EXPERIMENTAL METHODS

Single crystals of RFe_2Zn_{20} and RCo_2Zn_{20} (R =Y, Gd-Lu) were grown from high temperature Zn rich solutions with the initial concentration of starting elements being R:(Fe/Co):Zn=2:4:94, as described previously.[10,14] The small amount of residual Zn on the resulting crystals was removed by submerging the crystals into an ultrasonic bath of 0.5 vol % HCl in H_2O for 0.5–1 h. Attempts were made to grow even lighter rare-earth members (R=Eu, Nd, and Ce) for the Fe series, but no ternary compounds were found to form. On the other hand, for the Co series, single crystals for the R=Nd and Sm members were grown using the same method. Room temperature powder x-ray diffraction measurements, using Cu K_α radiation, were performed on the samples with additional Si powder (a=5.430 88 Å) used as standard. Figure 2 shows the lattice constants for the two series of compounds, obtained by using the RIETICA, Rietveld refinement program, plotted with respect to the effective radius of R^{3+} with CN=9 (Ref. 15) since the data are absent for larger CN. The variation in the lattice constant manifests the well known lanthanide contraction for R =Gd-Lu, with no evident deviation for R=Yb. However, the relatively larger lattice constants for YFe_2Zn_{20} and YCo_2Zn_{20} indicate that, with this large CN, the effective ionic radius of Y^{3+} is between Tb^{3+} and Dy^{3+} rather than between Dy^{3+} and Ho^{3+}. This deviation for Y^{3+} ions is not unprecedented, appearing in the isostructural compounds RRu_2Zn_{20} (Ref. 6) and $RMn_2In_xZn_{20-x}$,[16] as well as the similar structure compounds RCo_2.[17] Additional single-crystal x-ray diffraction measurements were preformed on R=Gd, Tb, Er, and Lu members of the RFe_2Zn_{20} series and demonstrated full occupancy on all crystallographic sites (within the detection errors) and the same lattice as the powder x-ray values.[18] This result is complicated by the difficulty in resolving the difference between Fe and Zn elements with very similar x-ray scattering strengths.

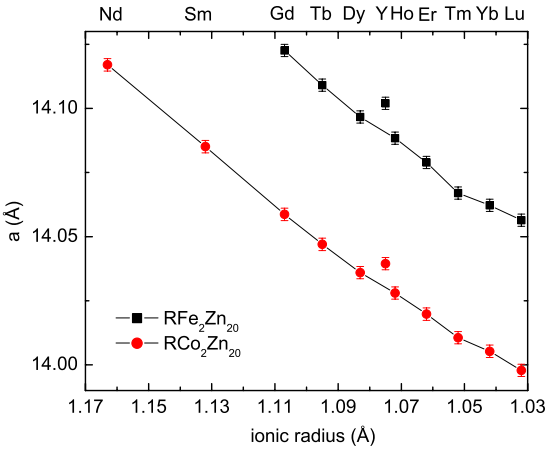

FIG. 2. (Color online) The lattice constants (a) for RFe_2Zn_{20} and RCo_2Zn_{20} versus the radius of the trivalent rare-earth ion with CN=9 (Ref. 15). The error bars were estimated from the standard variation in four separate measurement made on one batch of sample.

It is worth noting that for local moment bearing members in the Fe series, single crystals obtained from different ratios of starting element concentrations manifest detectably different magnetic ordering temperatures. These differences, tentatively associated with very subtle variations in element occupancy on the crystallographic sites,[19] are related to extreme sensitivity to a small amount of disorder for compounds with such strongly correlated conduction electron backgrounds. A detail discussion of this is presented in Appendix A.

Measurements of electrical resistivity were preformed by using a standard ac four-probe technique. The samples were cut into bars, with typical lengths of 2–3 mm, along their crystallographic [110] direction. These bars were measured in a Quantum Design physical property measurement system (PPMS), PPMS-14 and/or PPMS-9 instruments (T=1.85–310 K) with f=16 Hz and I=3–0.3 mA. Temperature-dependent specific heat measurements were

also performed in these PPMS units using the heat capacity option. In order to study the magnetic part of specific heat, the contribution from the conduction electrons and lattice vibrations was approximated and subtracted. This was performed by subtracting the specific heat of the nonmagnetic members YT_2Zn_{20} or LuT_2Zn_{20} $[C_{mag} = C_p(RT_2Zn_{20}) - C_p(Lu/YT_2Zn_{20})]$. The magnetic part of the entropy can then be estimated as $S_M = \int([C_p(RT_2Zn_{20}) - C_p(Lu/YT_2Zn_{20})]/T)dT$, in which the specific heat data below 1.8 K (0.4 K for $TmCo_2Zn_{20}$) were approximated by a linear extrapolation to $C_p = 0$ at 0 K.

Magnetization measurements were carried out in Quantum Design magnetic properties measurement system superconducting quantum interface device magnetometers in varied applied fields ($H \leq 55$ kOe) and temperatures ($T = 1.85-375$ K). In the measurements of magnetization for the FM-ordered RFe$_2$Zn$_{20}$ compounds, the effects of the demagnetizing field are relatively small because of the dilute nature of the magnetic moments:[12,13] the maximum demagnetizing field is about 3000 Oe for a platelike shaped sample. Even so, in order to obtain accurate magnetization isotherms near T_C, the samples were cut and measured with the applied field along their long axis so as to minimize this already small demagnetization effect.

III. RESULTS

We start by characterizing the compounds with nonmagnetic rare-earth ions: Y(Lu)Fe$_2$Zn$_{20}$ and Y(Lu)Co$_2$Zn$_{20}$. Without any 4f electronic magnetism, these compounds manifest the electronic and magnetic properties associated with the conduction electron background of each series. Next, we introduce the two series of compounds with well-defined 4f local moments: R=Gd-Tm. We examine the magnetization and specific heat data for the Co series at first. An overview of the magnetic properties for the Fe series is presented next. The magnetization, specific heat, and resistivity data are discussed for each Fe member separately. Finally, similar data for the R=Yb heavy fermion compounds, YbFe$_2$Zn$_{20}$ and YbCo$_2$Zn$_{20}$, are shown.

A. Y(Lu)Fe$_2$Zn$_{20}$ and Y(Lu)Co$_2$Zn$_{20}$

Temperature-dependent magnetization data (divided by the applied field) for Y(Lu)Fe$_2$Zn$_{20}$ and Y(Lu)Co$_2$Zn$_{20}$ are shown in Fig. 3(a). The Fe members manifest similar, strongly enhanced, temperature-dependent paramagnetic signals, whereas the Co members manifest essentially temperature-independent Pauli paramagnetic signals. The low temperature features for the two Fe compounds are shown in the inset of Fig. 3. In an applied field of 10 kOe, the magnetization signals of both Fe members show a faint maximum below 10 K, whereas the high magnetic field (50 kOe) suppresses the lowest temperature M/H values, as well as the maximum. In our experience on the measurements of different batches of samples, these low temperature features are moderately sample dependent (different samples may show up to 20% difference in magnetization signal and 2–3 K difference in the temperature of the maximum, T_{max}). Nevertheless, the maximum of the temperature-dependent susceptibility, $\chi(T)$, is a common feature in the NFFLs, such as Pd,[20] YCo$_2$, and LuCo$_2$,[21] as well as TiBe$_2$,[22] although quantitative calculation of $\chi(T)$ still presents a challenge even for the simplest case of Pd.[23,24] The field suppression of the magnetization (and T_{max}) at low temperature is not attributable to the possible existence of a paramagnetic impurity contribution (which would contribute more to the value of M/H at lower temperature and lower field and therefore suppress the maximum of M/H in lower field) but, as discussed below, to the intrinsic variation in $\chi = dM/dH$ with respect to H at different temperatures.

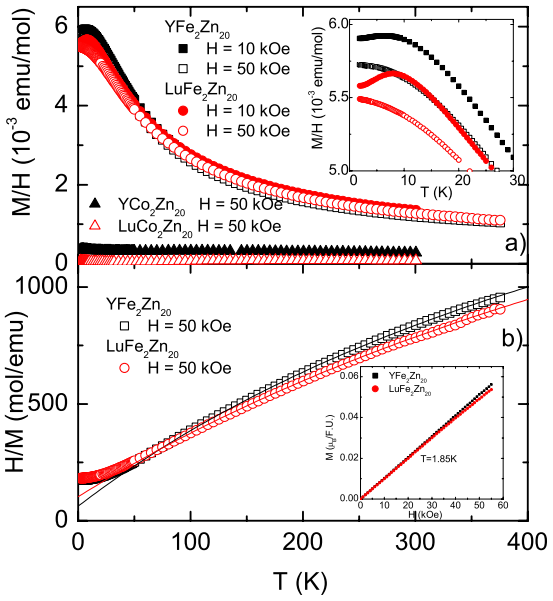

FIG. 3. (Color online) (a) Temperature-dependent magnetization M divided by the applied field H for YFe$_2$Zn$_{20}$ and LuFe$_2$Zn$_{20}$ as well as their Co analogs for H=10 and 50 kOe. Inset: a blow-up plot at low temperature. (b) H/M for YFe$_2$Zn$_{20}$ and LuFe$_2$Zn$_{20}$. The solid lines present the modified Curie-Weiss $[\chi(T) = C/(T-\theta_C) + \chi_0]$ fit for the data above 100 K. Inset: field-dependent magnetization at 1.85 K.

Figure 3(b) shows that above a characteristic temperature ($T^* \sim 50$ K), the susceptibility of YFe$_2$Zn$_{20}$ and LuFe$_2$Zn$_{20}$ can be approximately fitted by a Curie-Weiss (CW) term $[\chi(T) = C/(T-\theta_C)]$ plus a temperature-independent term (χ_0). The values of effective moment (μ_{eff}), θ_C, and χ_0 are extracted as $1.0\mu_B$/Fe, -16 K, 3.8×10^{-4} emu/mol and $1.1\mu_B$/Fe, -33 K, 3.4×10^{-4} emu/mol for YFe$_2$Zn$_{20}$ and LuFe$_2$Zn$_{20}$, respectively. These values of μ_{eff} are significantly larger than the estimated induced moment of Fe site in the FM ground state of GdFe$_2$Zn$_{20}$, $\sim 0.35\mu_B$/Fe.[10] Such apparent CW-like behavior has also been observed in other NFFL systems.[21,25] In the context of the spin fluctuation model,[3] itinerant electronic systems can manifest CW-like behavior with a Curie constant related to the local amplitude of the spin fluctuation. The magnetization data at the base temperature (1.85 K) show nearly linear dependence with the applied field [inset of Fig. 3(b)], which is distinct from the Brillouin function type of magnetization curves associated with local moments.

In order to better understand the variation in the maximum in temperature-dependent M/H data for YFe$_2$Zn$_{20}$ and

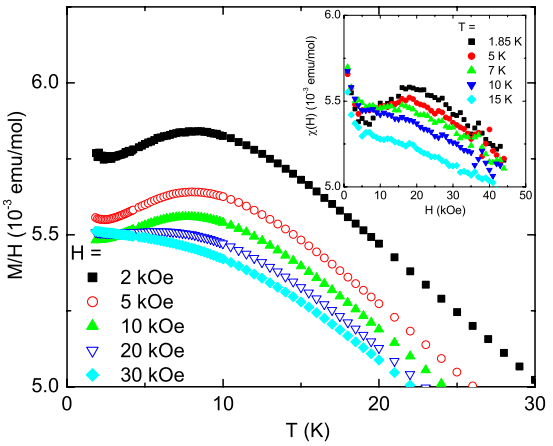

FIG. 4. (Color online) M/H for $LuFe_2Zn_{20}$. From right to left: $H=2$, 5, 10, 20, and 30 kOe. Inset: $\chi(H)$ for $LuFe_2Zn_{20}$ at varied temperature.

$LuFe_2Zn_{20}$, $M(T)$ and $M(H)$ measurements were performed on $LuFe_2Zn_{20}$ for various applied fields and temperatures, respectively. Figure 4 shows that the magnetic field suppresses the values of M/H, as well as the maximum of M/H, which disappears when $H \geq 20$ kOe. The values of the field-dependent susceptibility, $\chi(H)$, were extracted as $\chi(H) = \frac{M(H+\Delta H)-M(H)}{\Delta H}$ with $\Delta H = 1000$ Oe from the $M(H)$ data at varied temperature (inset of Fig. 4). For $T \geq 10$ K, the values of $\chi(H)$ monotonically decrease with increasing H, whereas a local maximum appears around 20 kOe in the data sets as $T \leq 7$ K. This critical temperature (~7 K) is close to the T_{max}; the maximum of $\chi(H)(H=20$ kOe) is also close to the suppression field determined by Fig. 4. This curious, field-dependent, susceptibility at varied temperature is reminiscent to the one of $TiBe_2$, albeit the amplitude of local maximum in $\chi(H)$ is much smaller.[22,26] In the case of $TiBe_2$, the reason of anomalous field-dependent magnetization is also still not clear.[27]

Figure 5 presents the low temperature specific heat data for YFe_2Zn_{20} and $LuFe_2Zn_{20}$, as well as for the Co analogs, plotted as C_p/T versus T^2. All four compounds manifest clear Fermi liquid behavior ($C_p = \gamma T + \beta T^3$). The similar β values (represented as the slopes of the data sets in the plot,

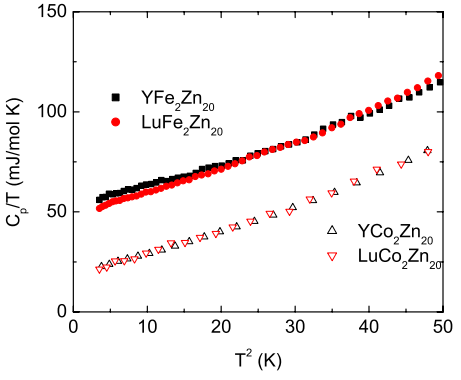

FIG. 5. (Color online) Low temperature specific heat data of YFe_2Zn_{20} and $LuFe_2Zn_{20}$ (plotted as C_p/T versus T^2), as well as the Co analogs.

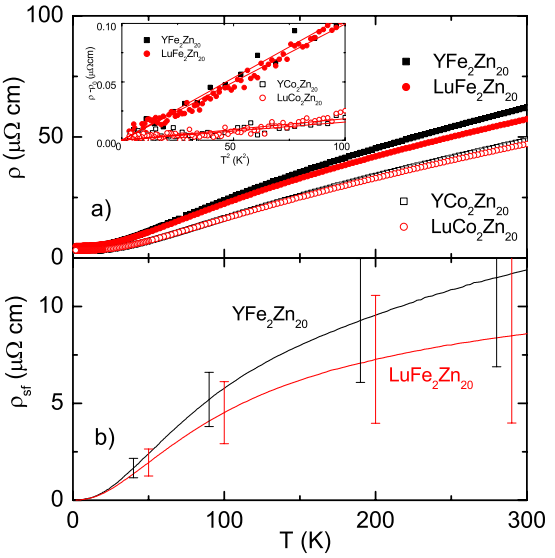

FIG. 6. (Color online) (a) Temperature-dependent resistivity of YFe_2Zn_{20} and $LuFe_2Zn_{20}$, as well as their Co analogs. Inset: ρ versus T^2. The solid lines present the linear fit of the data sets from 2 to 9 K. (b) Estimated spin fluctuation contribution to the resistivity for YFe_2Zn_{20} and $LuFe_2Zn_{20}$. The error bars were estimated as $\pm 10\%$ of the values of the resistivity for YCo_2Zn_{20} and $LuCo_2Zn_{20}$, respectively.

~1.2 mJ/mol K^4) indicate similar Debye temperatures for these four compounds [~340 K (Ref. 13)], consistent with their similar molar masses, composition, and lattice parameters. On the other hand, the larger values (over 2.5 times much) of electronic specific heat (γ) of the Fe members indicate a larger density of states at the Fermi level [$N(E_F)$] compared to the Co analogs (consistent with the band structure calculation results[13]).

The values of the electronic specific heat and magnetic susceptibility can be employed to estimate the Stoner enhancement factor, Z, in the context of the Stoner theory: the static susceptibility is enhanced by $\frac{1}{1-Z}$, whereas the electronic specific heat is not.[10] The estimated Z values of YFe_2Zn_{20} and $LuFe_2Zn_{20}$ are 0.88 and 0.89, respectively, comparable with the estimated values of the canonical NFFL systems: Pd: 0.83 and YCo_2: 0.75.[28]

The temperature-dependent electrical resistivity data for YFe_2Zn_{20} and $LuFe_2Zn_{20}$ are larger than that for the Co analogs over the whole temperature range [Fig. 6(a)]. This is not unexpected for a NFFL since the spin fluctuations will affect the scattering process of the conduction electrons, which leads to an additional contribution to the resistivity. In order to study the spin fluctuation contribution to the resistivity, the total electrical resistivity $\rho(T)$ is assumed to be

$$\rho(T) = \rho_0 + \rho_{ph}(T) + \rho_{sf}(T), \quad (1)$$

where the first, second, and third terms represent residual, phonon, and spin fluctuation resistivity, respectively. Assuming the phonon scattering contribution, $\rho_{ph}(T)$, is essentially the same for the Fe and Co analogs (as suggested by the similar β terms), then, the spin fluctuation scattering contribution, $\rho_{sf}(T)$, can be estimated as

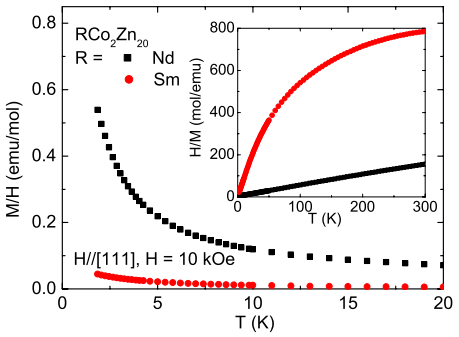

FIG. 7. (Color online) Temperature-dependent magnetization of RCo$_2$Zn$_{20}$ (R=Nd and Sm) compounds divided by applied field H =10 000 Oe. Inset: applied field (H=10 000 Oe) divided by the magnetizations of RCo$_2$Zn$_{20}$ (R=Nd and Sm) as a function of temperature.

$$\rho_{sf}(T) = (\rho - \rho_0)_{\mathrm{Y/LuFe_2Zn_{20}}} - (\rho - \rho_0)_{\mathrm{Y/LuCo_2Zn_{20}}}. \quad (2)$$

Shown in Fig. 6(b), $\rho_{sf}(T)$ for these two compounds increases with temperature and is close to a saturated value (10 $\mu\Omega$ cm) at 300 K, within the accuracy of the measurements.

Analysis of the low temperature resistivity data reveals a quadratic standard Fermi liquid behavior $[\rho(T)=\rho_0+AT^2]$ for all four compounds (inset of Fig. 6). The A values of the Fe compounds are about seven times larger than the two Co analogs. This result is consistent with the 2.5 times larger γ values of the Fe compounds in the context of the Fermi liquid theory, meaning A is proportional to the square of the effective mass of the quasiparticles due to the strong correlation effect, whereas γ is proportional to the effective mass. In the point of view of spin fluctuation theory, nearly FM metals manifest Fermi liquid behaviors at low temperatures with A values enhanced by spin fluctuations.[3]

B. RCo$_2$Zn$_{20}$ (R=Nd,Sm,Gd-Tm)

The results of thermodynamic measurement on NdCo$_2$Zn$_{20}$ and SmCo$_2$Zn$_{20}$ are briefly examined before discussing the heavy rare-earth compounds (R=Gd-Yb). Figure 7 shows the low temperature-dependent magnetization data (divided by the applied field H=1000 Oe) for NdCo$_2$Zn$_{20}$ and SmCo$_2$Zn$_{20}$. Neither of them displays any sign of magnetic ordering above 2 K. The temperature-dependent H/M for NdCo$_2$Zn$_{20}$ shows a CW behavior $[\chi(T)=C/(T-\theta_C)+\chi_0]$ with $\mu_{eff}=3.7\mu_B$, $\theta_C=-2.3$ K, and $\chi_0=6.8\times10^{-4}$ emu/mol. The value of the effective moment is close to the theoretical value for Hund's rule ground state of the 4f electrons of Nd^{3+} ion (3.6μ_B). On the other hand, though the magnetization of SmCo$_2$Zn$_{20}$ drops with increasing temperature, it does so in a distinctly non-CW manner. This behavior is not unexpected in Sm containing compounds[29] and is most likely due to the thermal population of the first excited Hund's rule multiplet.

Specific heat data for NdCo$_2$Zn$_{20}$ and SmCo$_2$Zn$_{20}$ are shown in Fig. 8 along with data for YCo$_2$Zn$_{20}$ for comparison. The low temperature upturn in the NdCo$_2$Zn$_{20}$ data below 2 K may be due to a lower temperature magnetic ordering or a Schottky anomaly due to the CEF splitting. The specific heat data for SmCo$_2$Zn$_{20}$ manifest a broad peak around 4 K, which is most likely due to the CEF splitting of Hund's rule ground state of Sm^{3+}. Both NdCo$_2$Zn$_{20}$ and SmCo$_2$Zn$_{20}$ data increase much faster above 10 K and remain more than 10 J/mol K larger above 25 K (not shown here) compared with the data for the nonmagnetic analog YCo$_2$Zn$_{20}$. On the other hand, the calculated results of the CEF splitting for Hund's rule ground state of Nd^{3+} ion in a point charge model show the splitting energy levels within 25 K (see Table II below). This large difference indicates that, at this point, the magnetic part of C_p for NdCo$_2$Zn$_{20}$ and SmCo$_2$Zn$_{20}$ cannot be well estimated since the C_p data of YCo$_2$Zn$_{20}$ may not an adequate approximation of the nonmagnetic background and unfortunately the LaCo$_2$Zn$_{20}$ analog does not form.

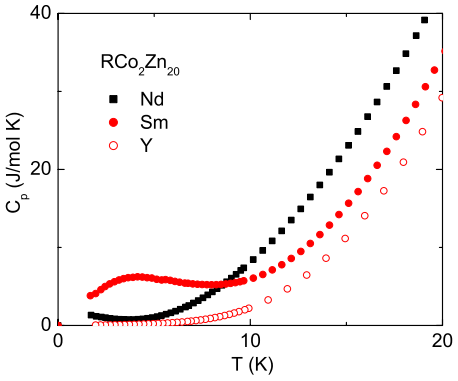

FIG. 8. (Color online) Temperature-dependent specific heat for RCo$_2$Zn$_{20}$ (R=Nd, Sm, and Y).

Temperature-dependent magnetization data (divided by the applied field H=1000 Oe) for RCo$_2$Zn$_{20}$ (R=Gd-Yb) are presented in Fig. 9. In addition to the previously reported AFM-ordered GdCo$_2$Zn$_{20}$ with Neél temperature T_N =5.7±0.1 K,[10,13] TbCo$_2$Zn$_{20}$ also shows AFM ordering with T_N=2.5±0.1 K, which also clearly manifests itself in the specific heat data (shown below in Fig. 11). The rest of the members (R=Dy-Yb) do not show magnetic ordering above 2 K. Due to the relatively low $N(E_F)$ for the Y and Lu analogs[10,13] and large R-R separation, such low temperature magnetic ordering for the 4f local moments coupled via the

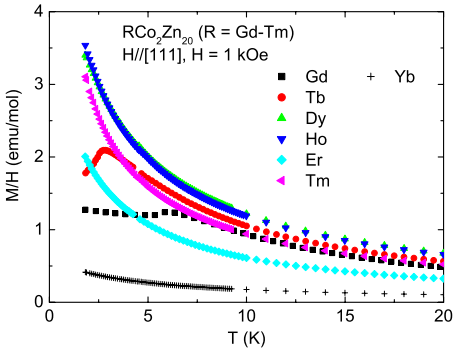

FIG. 9. (Color online) Temperature-dependent magnetization of RCo$_2$Zn$_{20}$ (R=Gd-Yb) compounds divided by applied field H =1000 Oe.

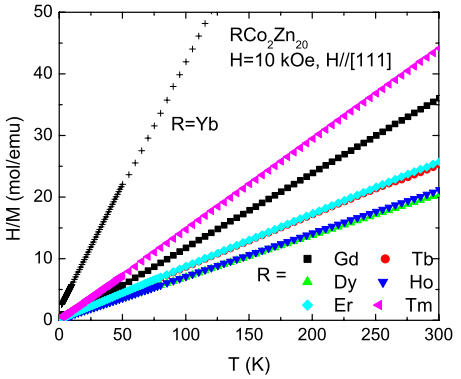

FIG. 10. (Color online) Applied field (H=10 000 Oe) divided by the magnetizations of $R\mathrm{Co_2Zn_{20}}$ (R=Gd-Yb) as a function of temperature.

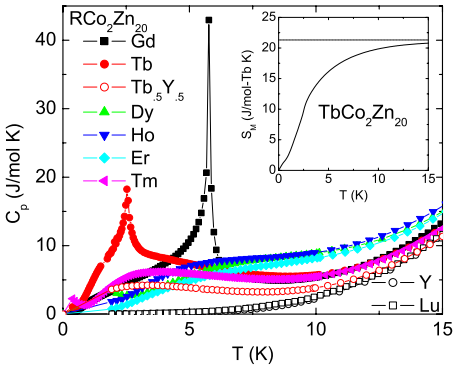

FIG. 11. (Color online) Temperature-dependent specific heat for $R\mathrm{Co_2Zn_{20}}$ (R=Gd-Tm, Y, and Lu), as well as $\mathrm{Tb_{0.5}Y_{0.5}Co_2Zn_{20}}$. Inset: temperature-dependent magnetic entropy for $\mathrm{TbCo_2Zn_{20}}$. The dashed line presents the entropy of the full Hund's ground state of Tb^{+3}.

Ruderman-Kitter-Kasaya-Yosida (RKKY) interaction is not unexpected.

Figure 10 shows the temperature-dependent H/M for R =Gd-Tm and Yb members of the $R\mathrm{Co_2Zn_{20}}$ series. All the members, including $\mathrm{YbCo_2Zn_{20}}$, manifest CW behavior $[\chi(T)=C/(T-\theta_C)+\chi_0]$ with negligibly small χ_0 ($\leq 2\times 10^{-3}$ emu/mol) and the values of μ_{eff} close to the theoretical values for Hund's ground state of the $4f$ electronic configurations. All the values of θ_C are close to 0, consistent with the low magnetic ordering temperatures (Table I).

The specific heat data for $R\mathrm{Co_2Zn_{20}}$ (R=Gd-Tm, Y, and Lu), as well as the pseudoternary compound $\mathrm{Tb_{0.5}Y_{0.5}Co_2Zn_{20}}$, are presented in Fig. 11. In addition to the previously studied $\mathrm{GdCo_2Zn_{20}}$, the specific heat data for $\mathrm{TbCo_2Zn_{20}}$ manifest a λ type of anomaly with a peak position at 2.5 K, the AFM ordering temperature. In addition to this peak, the C_p data also show a broad shoulder above 2.5 K, which is due to the CEF splitting above the magnetic ordering temperature. This anomaly, associated with CEF splitting of the $4f$ electronic configuration of Tb^{3+}, displays itself more clearly in the C_p data for $\mathrm{Tb_{0.5}Y_{0.5}Co_2Zn_{20}}$: when T_N is suppressed to well below 2 K, the C_p data show a Schottky anomaly with a peak position ~3 K. The magnetic contribution to the entropy for $\mathrm{TbCo_2Zn_{20}}$ is shown in the inset of Fig. 11. Approximately 50% of the total magnetic entropy is recovered by T_N and by 15 K the full $S_M=R\ln 13$ is recovered (where R is the gas constant). This is consistent with a very small total CEF splitting in these compounds, associated with the highly symmetric environment of the R ions. For the rest of the members, R=Dy-Tm, the C_p data show broad Schottky-type anomalies below 10 K, as shown in Fig. 13 below. The low temperature upturn for $\mathrm{DyCo_2Zn_{20}}$ data below 2 K may indicate a magnetic ordering at lower temperature, whereas the upturn for $\mathrm{TmCo_2Zn_{20}}$ data below 0.7 K may be associated with a magnetic ordering at very low temperature and/or a nuclear Schottky anomaly.

The magnetic part of the entropy above 2 K (above 0.4 K for the $\mathrm{TmCo_2Zn_{20}}$) is shown in Fig. 12. For R=Dy-Tm, there is an obvious deficit of magnetic entropy compared with the value associated with a fully degenerated Hund's ground state, which indicates unaccounted entropy below 2 K (0.4 K for $\mathrm{TmCo_2Zn_{20}}$) associated with low lying CEF levels and magnetic ordering.

In order to better understand the magnetic properties for R=Tb-Tm members, the CEF effect acting on the R ions is evaluated by thermodynamic measurements. The single-ion Hamiltonian for the R^{3+} is assumed to be the sum of the CEF term, an exchange interaction term, and an external field term,

$$\mathcal{H}=\mathcal{H}_{\mathrm{CEF}}+\mathcal{H}_{exc}+\mathcal{H}_{ext}, \tag{3}$$

where $\mathcal{H}_{ext}=g_J\mu_B\vec{J}\cdot\vec{H}$ (g_J is the Landé factor, $\vec{J}$ is the total angular momentum, and $\vec{H}$ is the external magnetic field).

Since the rare-earth ions are located in a cubic point symmetry, the CEF term, $\mathcal{H}_{\mathrm{CEF}}$, can be written as

$$\mathcal{H}_{\mathrm{CEF}}=B_4^0(O_4^0+5O_4^4)+B_6^0(O_6^0-21O_6^4), \tag{4}$$

where O_l^m operators are the well-known Stevens operators[30] and B_4^0 and B_6^0 are CEF parameters.[31] This expression can be written as

TABLE I. Paramagnetic Curie temperature θ_C (with ±0.1 K uncertainty), effective moment μ_{eff} [from the CW fit of $\chi(T)$ from 50 to 300 K], and Neél temperature T_N for $R\mathrm{Co_2Zn_{20}}$ compounds (R =Nd,Gd-Yb).

	Nd	Gd	Tb	Dy	Ho	Er	Tm	Yb
θ_C (K)	−2.3	3.3	−2.6	−3.7	1.4	−2.1	−0.9	−5.2
μ_{eff} (μ_B)	3.7	8.1	9.8	10.9	10.7	9.7	7.4	4.5
T_N (K)		5.7	2.5					

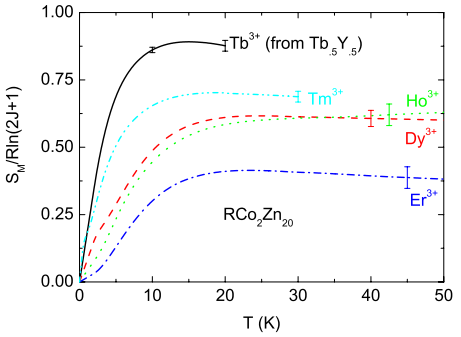

FIG. 12. (Color online) Normalized magnetic part of entropy for RCo$_2$Zn$_{20}$ (R=Dy-Tm) as well as for Tb$_{0.5}$Y$_{0.5}$Co$_2$Zn$_{20}$ (in units of per mole R^{3+}). The error bars were estimated from the ±1% of the total entropy.

$$\mathcal{H}_{\mathrm{CEF}} = W\left[\frac{x}{F4}(O_4^0 + 5O_4^4) + \frac{1-|x|}{F6}(O_6^0 - 21O_6^4)\right], \quad (5)$$

where $F4$ and $F6$ are factors introduced by Lea *et al.*[31] and are dependent on J, W is the energy scale, and x represents the relative importance of the fourth and sixth order terms.

Noticing that the possible magnetic ordering temperatures are below 2 K for RCo$_2$Zn$_{20}$ (R=Dy-Tm), as well as for Tb$_{0.5}$Y$_{0.5}$Co$_2$Zn$_{20}$, the exchange interaction term can be approximated as zero, which will be better for R=Tm than for R=Dy. Thus, the CEF parameters for different R ions were determined by fitting the magnetization at 2 K and the temperature-dependent specific heat data.

Figure 13 shows data and CEF fitting results of the magnetic part of specific heat with the single-ion Hamiltonian (ignoring the interaction term) for Tb$_{0.5}$Y$_{0.5}$Co$_2$Zn$_{20}$ and RCo$_2$Zn$_{20}$ (R=Dy-Tm). The specific heat data for all members are less than that of YCo$_2$Zn$_{20}$ above 30 K, which is likely due to the errors associated with resolving the difference between the sample's total C_p and the relatively large nonmagnetic contribution. Therefore, the fittings of C_M were performed below 20 K. As shown in Table II, the inferred W and x values for all five compounds are clustered in a narrow range: $|W|<0.1$, $|x|<0.25$. This result, indicating small energy scales of the CEF effect and relatively large B_6^0 terms, is

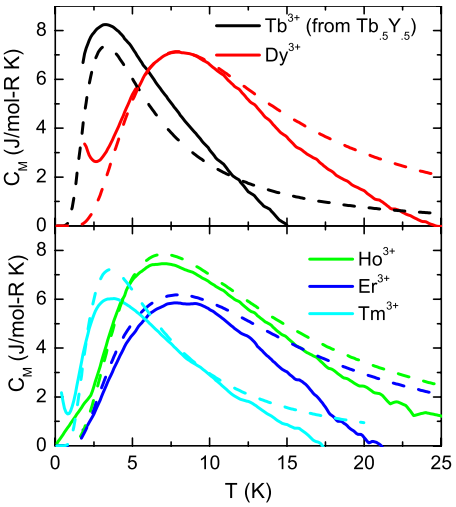

FIG. 13. (Color online) Magnetic part of specific heat for RCo$_2$Zn$_{20}$. The solid and dashed line present the experimental and calculated results, respectively.

roughly consistent with the calculated results based on the point charge model (see Appendix B). Furthermore, it should be noted that the signs of the B_6^0 terms for the calculated results are all consistent with the experimental ones; this is not the case for the B_4^0 terms. This behavior is not difficult to understand: as shown in Appendix B, the contributions to the CEF splitting are mainly from the CN-16 Frank-Kasper polyhedron formed by 4 NN and 12 NNN Zn neighbors. For the B_4^0 term, the contributions of the two sets of neighbors cancel each other, whereas the contribution for the B_6^0 terms is the sum. Therefore, the net B_6^0 term is relatively large and the calculated results are more reliable.

C. RFe$_2$Zn$_{20}$ (R=Gd-Tm)

Before discussing each of the compounds in this series separately, an overview of their temperature-dependent magnetization data serves as a useful point of orientation. Figure 14 shows M/H versus T (the applied field H=1000 Oe) for R=Gd-Tm members. In contrast to the Co series compounds, the Fe series compounds all manifest FM ground states with

TABLE II. Comparison of the CEF parameters of RCo$_2$Zn$_{20}$ compounds (R=Nd, Tb-Yb) determined from magnetization measurements to those calculated in a point charge model.

		Nd	Tb	Dy	Ho	Er	Tm	Yb
Easy axis at 2 K	Expt.		[110]	[111]	[110]	[111]	[110]	[100]
W (K)	Expt.		0.084	−0.073	0.067	−0.077	0.07	
	Calc.	0.28	0.026	−0.021	0.018	−0.025	0.044	−0.28
x	Expt.		0.2	0.1	0.22	−0.1	−0.15	
	Calc.	0.26	−0.68	−0.41	0.23	−0.22	−0.41	−0.64
B_4^0 (10^{-4} K)	Expt.		2.8	−1.2	2.5	1.3	1.75	
	Calc.	12.2	−3.0	1.4	0.7	−0.9	−3.0	29.6
B_6^0 (10^{-4} K)	Expt.		8.9	−4.7	3.8	−5	7.9	
	Calc.	81.2	1.1	−0.9	1.0	−1.4	3.5	−81.4

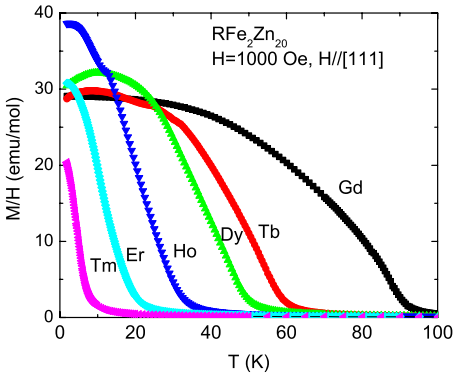

FIG. 14. (Color online) Temperature-dependent magnetization of $R\mathrm{Fe_2Zn_{20}}$ (R=Gd-Tm) divided by applied field $H=1000$ Oe.

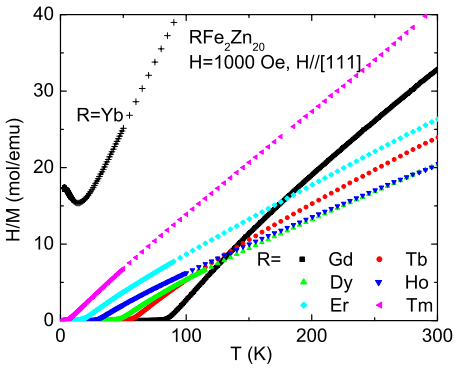

FIG. 15. (Color online) Applied field ($H=1000$ Oe) divided by the magnetizations of $R\mathrm{Fe_2Zn_{20}}$ (R=Gd-Tm) as a function of temperature.

enhanced T_C values, which systematically decrease as R varies from Gd to Tm. Such enhanced FM ordering has been explained as the result of local moments embedded in the NFFL host, most clearly seen in $\mathrm{YFe_2Zn_{20}}$ and $\mathrm{LuFe_2Zn_{20}}$.[10] This systematic variation in T_C on R is not unexpected for such heavy rare-earth compounds when the magnetic interaction between the R ions is associated with the spin part of Hund's ground state of $4f$ electrons.

The temperature-dependent H/M data, approximately equaling inverse susceptibilities $[1/\chi(T)]$ in the paramagnetic state, for R=Gd-Tm, as well as for $\mathrm{YbFe_2Zn_{20}}$, are shown in Fig. 15. Similar to $\mathrm{GdFe_2Zn_{20}}$,[10] the $1/\chi(T)$ data sets for R=Tb-Tm follow the CW law $[\chi(T)=C/(T-\theta_C)+\chi_0]$ at high temperatures and deviate from the law when approaching their magnetic ordering. The effective moments (μ_{eff}) and the paramagnetic Curie temperatures (θ_C) for these six compounds are listed in Table III. All μ_{eff} values are close to the theoretical value for Hund's ground state of the trivalent $4f$ electronic configuration.

1. $\mathrm{TbFe_2Zn_{20}}$

Temperature-dependent specific heat and resistivity data sets for $\mathrm{TbFe_2Zn_{20}}$ are shown in Fig. 16. The magnetic phase transition manifests as a faint feature in C_p data, indicating $T_C=56\pm3$ K. This is clearer in the magnetic specific heat (C_M) data (Fig. 16, left inset) where T_C is taken as the position of the greatest upward slope. As shown in the right inset to Fig. 16(b), at T_C the magnetic entropy is close to the value for the full degeneracy of Hund's ground state of Tb^{3+}, $R\ln 13$. For the rest of the local moment members (R=Dy-Er), the released magnetic entropy at T_C for the respective rare-earth ion is close to the full degeneracy value for their Hund's ground state. (There is significantly less for R=Tm.) The $\rho(T)$ data manifest as a change in slope, which can be seen even more clearly in the $d\rho/dT$ data, consistent with a $T_C=56\pm1$ K.

The inset of Fig. 17 presents a plot of M^2 versus H/M (an Arrott plot) isotherms near T_C. The isotherm that most closely goes though the origin is the one closest to T_C, giving a value of 58 K in this case, consistent with the results of the C_p and $\rho(T)$ measurements. Figure 17 shows magnetization versus external field data at 2 K along three different crystallographic directions: [100], [110], and [111]. All of these data sets are consistent with a low temperature FM ground state with moderate anisotropy. The spontaneous longitudinal magnetic moments in zero applied external field, estimated by the extrapolation of the magnetization curves to $H=0$, yield $M([110])=8.0\mu_B$, $M([111])=6.6\mu_B$, and $M([100])=5.7\mu_B$. Their ratio is very close to $1:\sqrt{2/3}:\sqrt{1/2}$. Such behavior indicates that the spontaneous magnetic moments along [111] and [100] directions can be understood as the projection of the one along the easy axis ([110]). At 2 K and 55 kOe, the saturated moment along the easy axis is $8.1\mu_B$, $0.9\mu_B$ less than the value associated with Hund's ground state.

2. $\mathrm{DyFe_2Zn_{20}}$

The specific heat data of $\mathrm{DyFe_2Zn_{20}}$ show a kink associated with magnetic ordering [Fig. 18(a)], which can be seen

TABLE III. Residual resistivity ratio, $RRR=R(300\ \mathrm{K})/R(2\ \mathrm{K})$, paramagnetic Curie temperature θ_C (with ±0.5 K errors), effective moment μ_{eff} [from the CW fit of $\chi(T)$ from 100 to 300 K, except for $\mathrm{GdFe_2Zn_{20}}$, which was fitted from 200 to 375 K (Ref. 13)], Curie temperature T_C, and saturated moment at 55 kOe along the easy direction μ_{sat} for $R\mathrm{Fe_2Zn_{20}}$ compounds (R=Gd-Yb).

	Gd	Tb	Dy	Ho	Er	Tm	Yb
RRR	8.1	7.2	15.0	10.0	13.2	10.1	31.2
θ_C (K)	46	30	20	9	0	−2	−23
μ_{eff} (μ_B)	7.9	9.5	10.5	10.6	9.5	7.7	4.7
T_C (K)	86	58	46	28	17	5.5	
μ_{sat} (μ_B)	6.7	8.1	9.5	9.9	8.5	6.2	

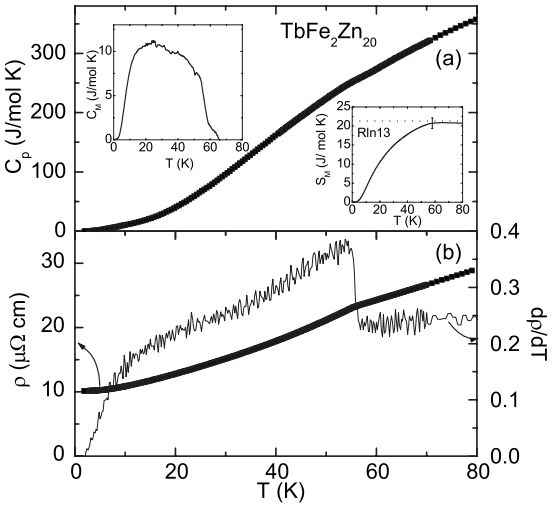

FIG. 16. (a) C_p for $TbFe_2Zn_{20}$; (b) ρ and $d\rho/dT$. Left inset: magnetic part of C_p; right inset: magnetic entropy S_M.

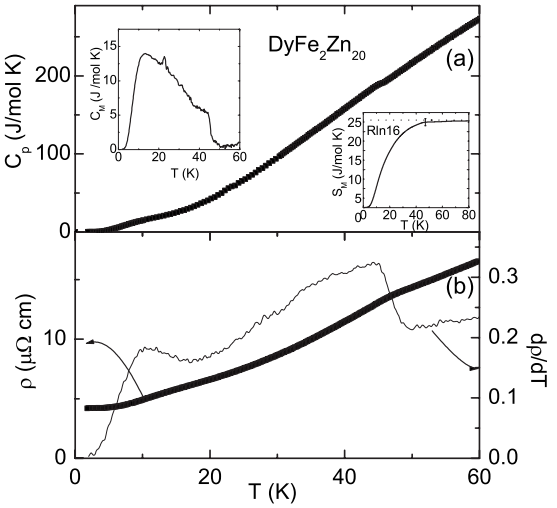

FIG. 18. (a) C_p for $DyFe_2Zn_{20}$; (b) ρ and $d\rho/dT$. Left inset: magnetic part of C_p; right inset: magnetic entropy S_M.

more clearly after the subtraction of the nonmagnetic background (left inset) and indicates $T_C=45\pm1$ K. This FM transition temperature is further confirmed by a weak change in slope in $\rho(T)$ (associated with the low temperature loss of spin disorder scattering), indicating $T_C=45\pm2$ K [Fig. 18(b)]. Given that the loss of spin disorder scattering in intermetallics often scales with de Gennes parameter,[32] the feature we find in $\rho(T)$ below T_C becomes fainter as R progresses from Gd to Tm. The value of T_C is consistent with the result of the Arrott plot analysis, from which a value of $T_C=45\pm1$ K can be inferred (inset of Fig. 19).

It is worth noting that the specific heat data show a faint shoulder near 10 K, which appears to be a broad peak after the background subtraction and is coincident with a slope change feature in $\rho(T)$ data. As seen below, such an anomaly below T_C in C_p and $\rho(T)$ data also appears for the R=Ho, Er, and Tm members. Those anomalies are likely due to the magnetic excitation energy spectrum associated with Hund's rule multiplet of R^{3+} ions in their FM states. (Further discussion will be presented below.)

The 2 K field-dependent magnetization isotherms for $DyFe_2Zn_{20}$ are shown in Fig. 19. Compared to $TbFe_2Zn_{20}$, the magnetization curves for $DyFe_2Zn_{20}$ reveal a slightly more complicated anisotropic behavior. The magnetization along the [100] direction manifests a metamagnetic phase transition near 12 kOe. Above this transition, the magnetization along the [100] direction is essentially the same as that for the field along the easy [111] axis. The spontaneous longitudinal magnetization along the three directions, $M([111])=9.1\mu_B$, $M([110])=7.4\mu_B$, and $M([100])=5.3\mu_B$, has a ratio very close to $1:\sqrt{1/2}:\sqrt{1/3}$. These results indicate that $M([110])$ and $M([100])$ can be seen as projections of $M([111])$. The metamagnetic phase transition along [100] can be understood as a classical spin reorientation in a cubic symmetry coordination. As in the case of $GdFe_2Zn_{20}$ and $TbFe_2Zn_{20}$, the saturated moment of $DyFe_2Zn_{20}$ at 55 kOe

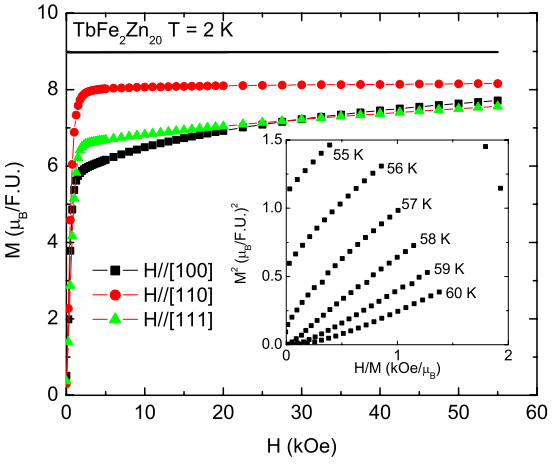

FIG. 17. (Color online) Field-dependent magnetization of $TbFe_2Zn_{20}$ along the three principle axes at 2 K. The three lines represent the calculated results based on molecular field approximation (all being clustered near $9\mu_B$ and appearing as a single line). Inset: Arrott plot of magnetic isotherms for $TbFe_2Zn_{20}$.

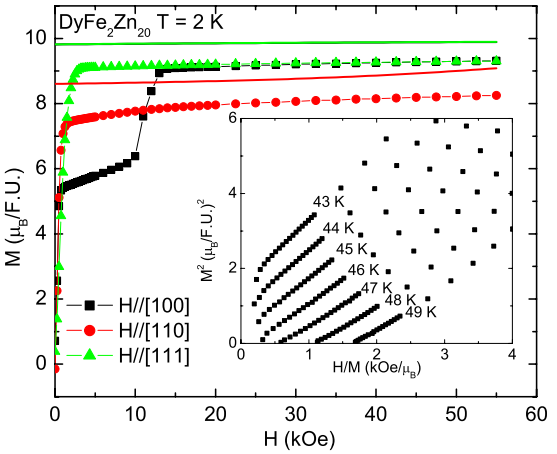

FIG. 19. (Color online) Field-dependent magnetization of $DyFe_2Zn_{20}$ at 2 K along the three principle axes. The solid lines represent the calculated result. Inset: Arrott plot of magnetic isotherms for $DyFe_2Zn_{20}$.

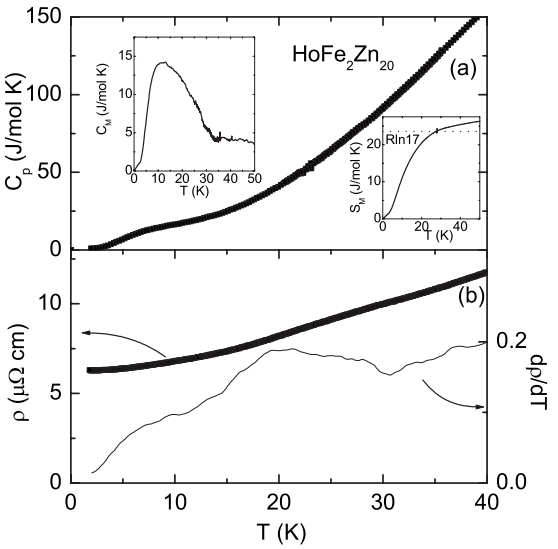

FIG. 20. (a) C_p for $HoFe_2Zn_{20}$; (b) ρ and $d\rho/dT$. Left inset: magnetic part of C_p; right inset: magnetic entropy S_M.

$(9.5\mu_B)$ is slightly less than the value of Hund's ground state value $(10\mu_B)$.

3. $HoFe_2Zn_{20}$

The anomalies associated with the FM transition in $HoFe_2Zn_{20}$ in the specific heat and resistivity data are relatively weak (Fig. 20). The specific heat anomaly can be associated with $T_C \sim 28$ K, and the $d\rho/dT$ data show a faint anomaly at this temperature (Fig. 20). The T_C value is determined as 28 ± 1 K from C_p data, as well as 29 ± 1 K from $\rho(T)$ data. This T_C value is consistent with the result of the Arrott plot analysis (inset of Fig. 21), which gives $T_C = 28 \pm 1$ K.

The low temperature magnetic isotherms for $HoFe_2Zn_{20}$ (Fig. 21) display similar but larger anisotropy to the ones for $TbFe_2Zn_{20}$. The ratio of the spontaneous magnetization

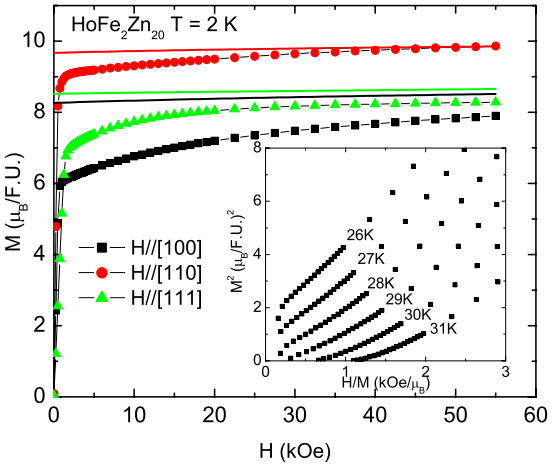

FIG. 21. (Color online) Field-dependent magnetization of $HoFe_2Zn_{20}$ at 2 K along the three principle axes. The solid lines represent the calculated result. Inset: Arrott plot of magnetic isotherms for $HoFe_2Zn_{20}$.

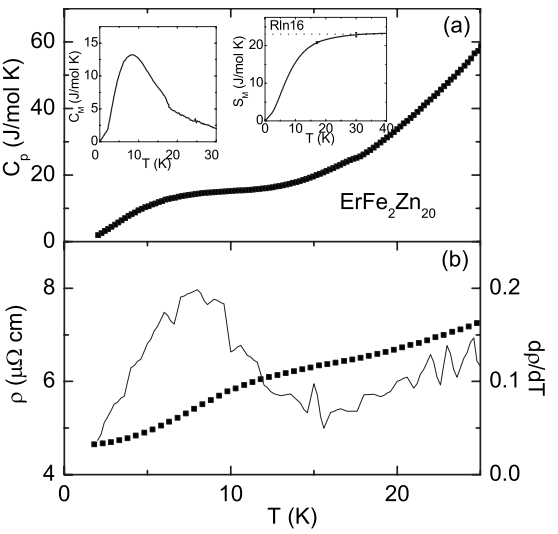

FIG. 22. (a) C_p for $ErFe_2Zn_{20}$; (b) ρ and $d\rho/dT$. Left inset: magnetic part of C_p; right inset: magnetic entropy S_M.

$[M([110]):M([111]):M([100]) = 9.1\mu_B:7.0\mu_B:6.1\mu_B]$ is close to the ratio of $1:\sqrt{2/3}:\sqrt{1/2}$. This ratio is consistent with the projection of the local moment from the easy [110] axis onto the [111] and [100] axes. In an external field of 55 kOe, the magnetization along the easy axis, ([110]), reaches a value of $9.9\mu_B$, very close to the value of Hund's ground state $(10\mu_B)$.

4. $ErFe_2Zn_{20}$

The specific heat and transport properties of $ErFe_2Zn_{20}$ are shown in Fig. 22. The specific heat data show a kink near 18 K [Fig. 22(a)], which can be seen more clearly after the background subtraction (left inset) and indicates $T_C = 18 \pm 1$ K. The resistivity data show no clear anomaly at this temperature (Fig. 22). The released magnetic entropy reaches 21 J/mol K at T_C, 90% of that associated with Hund's ground state of Er^{3+}, R ln 16 (Fig. 22, right inset). Although $\rho(T)$ data show no anomaly at T_C, we will see that the weak anomaly associated with magnetic ordering can be blown up after the background [$\rho(T)$ for $LuFe_2Zn_{20}$] is subtracted. The Arrott plot for $ErFe_2Zn_{20}$ (inset of Fig. 23), although showing nonlinear isothermal curves, demonstrates $T_C = 17 \pm 0.5$ K with little ambiguity. The nonlinear feature is not unexpected for the $4f$ local moment systems associated with the CEF induced anisotropy.[33]

The magnetic anisotropy of $ErFe_2Zn_{20}$ is reminiscent of that of $DyFe_2Zn_{20}$: both have the same easy and hard magnetization orientations, [111] and [110], respectively, as well as a metamagnetic transition along the [100] direction (Fig. 23). The ratio of the spontaneous longitudinal magnetic moments $[M([111]):M([110]):M([100]) = 7.4\mu_B:5.9\mu_B:4.2\mu_B]$ is also close to the ratio of $1:\sqrt{2/3}:\sqrt{1/3}$.

5. $TmFe_2Zn_{20}$

The specific heat data for $TmFe_2Zn_{20}$ have only one broad peak at 4.5 K [Fig. 24(a)], which is less like the anomalies

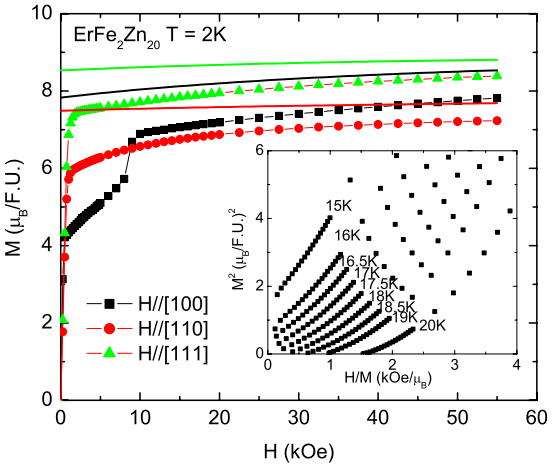

FIG. 23. (Color online) Field-dependent magnetization of $ErFe_2Zn_{20}$ at 2 K along the three principle axes. The solid lines represent the calculated result. Inset: Arrott plot of magnetic isotherms for $ErFe_2Zn_{20}$.

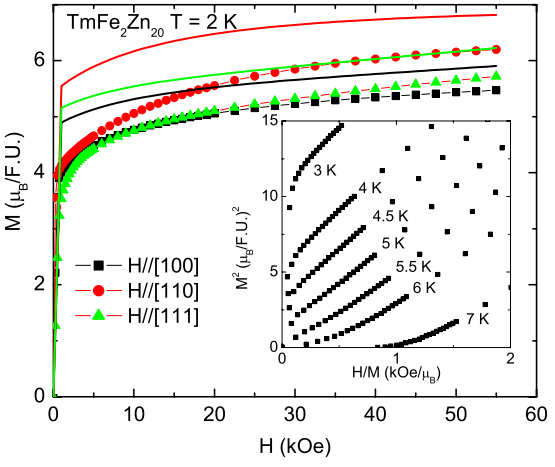

FIG. 25. (Color online) Field-dependent magnetization of $TmFe_2Zn_{20}$ at 2 K. The solid lines represent the calculated result. Inset: Arrott plot of magnetic isotherms for $TmFe_2Zn_{20}$.

associated with T_C for R=Gd-Er and more like a Schottky anomaly associated with a CEF splitting. The resistivity data also show an anomaly below 5 K [Fig. 24(b)], but at this point it is difficult to determine whether this anomaly is associated with the magnetic ordering or the CEF splitting of the $4f$ electrons of the Tm^{3+} ions. As we can see below, after the subtraction of the nonmagnetic background, the anomaly associated with the loss of the spin disorder scattering can be seen more clearly.

For $TmFe_2Zn_{20}$, the Arrott plot analysis provides the most reliable criterion for T_C determination. The inset of Fig. 25 shows that T_C can be determined as 5.5 ± 0.5 K without any ambiguity. At this temperature, the magnetic entropy is 15 J/mol K, only 70% of the value of the fully released entropy of Hund's ground state of Tm^{3+}, R ln 13 (Fig. 24, right inset).

The low temperature magnetic isotherms for $TmFe_2Zn_{20}$ manifest the same easy and hard axes as Tb and Ho members ([110] and [111], respectively) (Fig. 25). The spontaneous longitudinal magnetic moments along the three principle axes are all close to $4\mu_B$. This result may be due to the relatively low value of T_C, which makes the spontaneous magnetic moment less anisotropic at 2 K. The saturated moment along the easy axis reaches $6.2\mu_B$ at 55 kOe, $0.8\mu_B$ less than the value of Hund's ground state, $7\mu_B$.

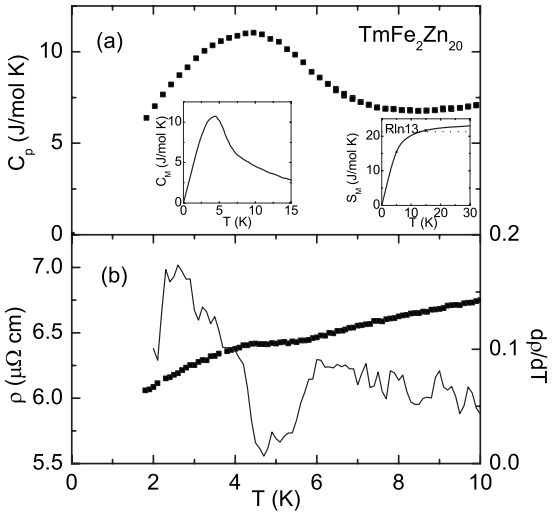

FIG. 24. (a) C_p for $TmFe_2Zn_{20}$; (b) ρ and $d\rho/dT$. Left inset: magnetic part of C_p; right inset: magnetic entropy S_M.

D. $YbFe_2Zn_{20}$ and $YbCo_2Zn_{20}$

The physical properties of $YbFe_2Zn_{20}$ and $YbCo_2Zn_{20}$ have been discussed in Ref. 11. They manifest typical heavy Fermion behavior with large electronic specific heat, 520 and 7900 mJ/mol K^2, respectively. Figure 26 shows temperature-dependent susceptibility and resistivity data for these two Yb compounds. The susceptibility data for $YbFe_2Zn_{20}$ manifest a broad Kondo-type peak about 20 K, indicating a clear loss of local moment behavior, whereas the susceptibility for $YbCo_2Zn_{20}$ shows CW behavior down to 1.8 K (Fig. 10), associated with the effective moment value μ_{eff}=4.5μ_B. Above ~50 K, $\chi(T)$ for $YbFe_2Zn_{20}$ displays a

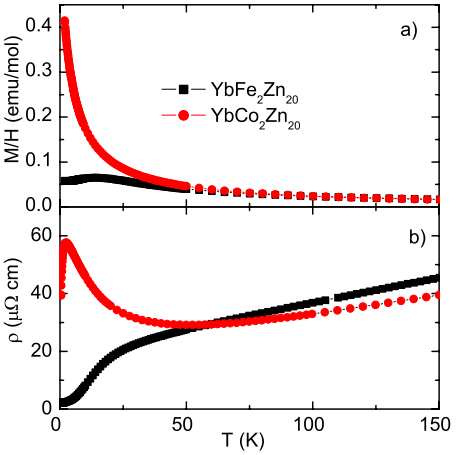

FIG. 26. (Color online) (a) Temperature-dependent M/H and (b) resistivity for $YbFe_2Zn_{20}$ and $YbCo_2Zn_{20}$ (H=1000 Oe).

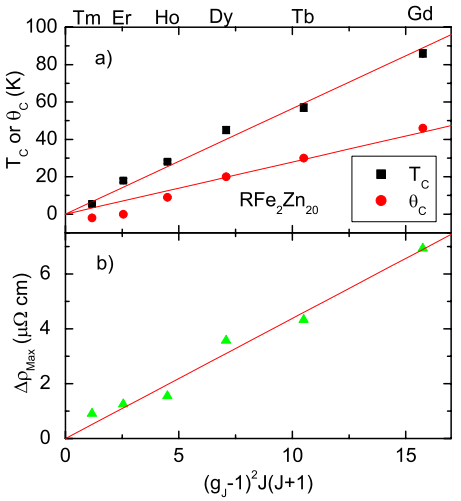

FIG. 27. (Color online) (a) T_C and θ_C, the maximum value on $\Delta\rho$ (b) with respect to the de Gennes factor for RFe$_2$Zn$_{20}$ (R=Gd-Tm).

CW behavior with an effective moment of $4.7\mu_B$, close to the value of Hund's ground state of Yb^{3+}, $4.5\mu_B$ (see Fig. 15). The resistivity data for YbFe$_2$Zn$_{20}$ show a broad shoulder about 30 K, whereas for YbCo$_2$Zn$_{20}$, the resistivity data show a Kondo resistance minimum about 50 K and a clear coherent peak around 2 K. These apparently different behaviors for these two Yb-based heavy fermion compounds with virtually identical structures have been explained as the result of significantly different Kondo temperatures: T_K=33 and 1.5 K for Fe and Co compounds, respectively.

IV. DATA ANALYSIS AND DISCUSSION

As shown in Fig. 27(a), the T_C values of RFe$_2$Zn$_{20}$ compounds (R=Gd-Tm) scale fairly well with the de Gennes factor, $dG=(g_J-1)^2J(J+1)$, consistent with an RKKY interaction. The θ_C values for the compounds are smaller than their respective T_C values (for R=Er and Tm, the values of θ_C are even negative). These small θ_C values are consistent with the deviation of $\chi(T)$ from the CW law (Fig. 15). As observed in the case of pseudoternary compounds $Gd_xY_{1-x}Fe_2Zn_{20}$, such deviation can be explained as a result of increasing coupling between the local moments embedded in the strongly temperature-dependent, polarizable matrix, YFe$_2$Zn$_{20}$ or LuFe$_2$Zn$_{20}$.[10]

Previous studies show that the magnetization of GdFe$_2$Zn$_{20}$ at base temperature is nearly isotropic, with a slightly reduced saturated moment ($\sim 0.5\mu_B$ less than the value of Hund's rule ground state of Gd^{3+}). For R=Tb-Tm, the magnetization anisotropy at base temperature is significant and correlates with the easy and hard axes of the respective RCo$_2$Zn$_{20}$ analogs. This behavior indicates that the anisotropy of the RFe$_2$Zn$_{20}$ (R=Tb-Tm) compounds may mainly be due to the CEF effect on the R^{3+} ions. The $M(H)$ curves at 2 K manifest divided behavior with non-Kramer ion (R=Tb, Ho, and Tm) on one hand and Kramer ion (R=Dy and Er) on the other: for R=Tb, Ho, and Tm, the magnetization processes are gradual along all three principal axes; for R=Dy and Er, the magnetization data along the [100] direction shows a clear and sharp metamagnetic transition. Both types of magnetization processes (gradual increase and metamagnetic transition) are common for the FM-ordered $4f$ local moments with CEF anisotropy associated with the R in a cubic point symmetry and can be understood in terms of the purification of the CEF split $4f$ electronic wave function due to the Zeeman effect of the external field and the rotation of the local moment.[34] Given that Tb^{3+} and Tm^{3+}, as well as Dy^{3+} and Er^{3+} ions have same total $4f$ electronic Hund's rule ground state quantum number ($\mathbf{J}$=6 and 15/2, respectively), the similar magnetic anisotropy indicates similar CEF effect for the two sets of rare-earth ions, respectively.

In order to better understand the magnetic anisotropy of RFe$_2$Zn$_{20}$ compounds (R=Tb-Tm), the CEF effect acting on the R ions must be considered. However, multiple difficulties associated with the strongly polarizable background [Y(Lu)Fe$_2$Zn$_{20}$], as well as the strong magnetic interaction, make the determination of the CEF parameters hard. For example, in order to reduce the magnetic interaction, the magnetic R^{3+} ions were placed into a dilute coordination, $R_xY_{1-x}Fe_2Zn_{20}$ or $R_xLu_{1-x}Fe_2Zn_{20}$. A FM ground state has been found even for very dilute magnetic R concentration: $Tb_{0.05}Y_{0.95}Fe_2Zn_{20}$, $Dy_{0.05}Y_{0.95}Fe_2Zn_{20}$, and $Ho_{0.1}Y_{0.9}Fe_2Zn_{20}$ manifest FM ordering above 2 K. For such small x, the background subtraction (magnetization and/or specific heat of YFe$_2$Zn$_{20}$ or LuFe$_2$Zn$_{20}$), as well as the uncertainty of x, makes the fitting process unreliable.

On the other hand, due to the very similar R coordination and the lattice parameters for Fe and Co series, the CEF parameters determined from RCo$_2$Zn$_{20}$ compounds should be close to those for the RFe$_2$Zn$_{20}$ compounds for respective R members. This assumption is consistent with the magnetic measurements for the pseudoternary Fe compounds, $Er_{0.1}Y_{0.9}Fe_2Zn_{20}$ and $Tm_{0.1}Y_{0.9}Fe_2Zn_{20}$. Manifesting a paramagnetic state at 2 K, their anisotropic magnetization isotherms show the same easy and hard axes as the calculated results from the determined CEF parameters of the Co compounds.

The magnetizations along the three axes for all Fe compounds were calculated based on the molecular field approximation in a self-consistent manner. In the single-ion Hamiltonian for the R^{3+} ions [Eq. (3)], with the molecular field approximation, the magnetic interaction term is written as

$$\mathcal{H}_{exc} = g_J\mu_B\vec{J}\cdot\vec{H}_M, \tag{6}$$

where H_M is the molecular field. It obeys the self-consistent condition

$$H_M = \lambda g\mu_B\langle\vec{J}\rangle, \tag{7}$$

$$\langle\vec{J}\rangle = \frac{\sum_0 J_n \exp(-E_n/k_BT)}{\sum_0 \exp(-E_n/k_BT)}, \tag{8}$$

where J_n and E_n are the eigenvalues and eigenenergies of the nth eigenfunction and λ is the molecular field constant

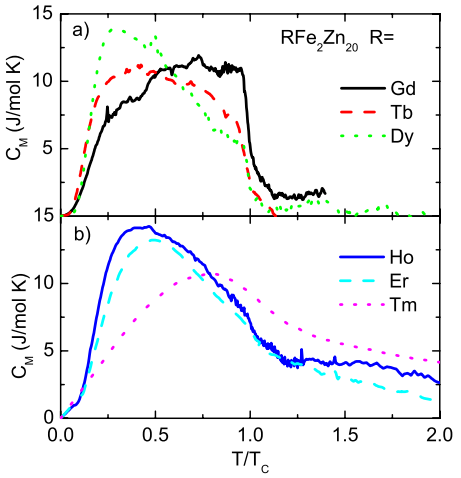

FIG. 28. (Color online) Magnetic part of specific heat versus T/T_C for RFe$_2$Zn$_{20}$ (R=Gd-Tm).

which can be obtained from the ordering temperature: $\lambda = 3k_B T_C/\mu_{eff}^2$.

The calculated magnetizations were compared with the experimental results as shown in Figs. 17, 19, 21, 23, and 25. All these calculated magnetization values are obviously larger than the experimental results. This difference is probably due to (i) the molecular field approximation overestimating the molecular field constant as well as the internal field and (ii) the induced moments from the Fe site aligning in an antiparallel manner with respect to the R^{3+} local moments [as in the case of GdFe$_2$Zn$_{20}$ (Ref. 10)].

Figure 28 shows the magnetic part of specific heat as a function of T/T_C for RFe$_2$Zn$_{20}$ (R=Gd-Tm). The magnetic ordering temperature (T_C) of R=Gd-Er members manifests itself as the position of maximum slope, with a decreasing sharpness as R varies from Gd to Er. TmFe$_2$Zn$_{20}$ does not appear to have any sharp anomaly in the C_M data at T_C. Below T_C, the data sets for R=Dy-Tm show a broad peak, which shifts closer to its T_C as R varies from Dy to Tm, whereas the data for GdFe$_2$Zn$_{20}$ show no explicit peak. If the broad peaks correspond to the magnetic excitation energy spectrum associated with CEF effect, then the relative positions of these peaks to T_C to some extent indicate the ratio of the energy scales of the CEF splitting (for a single ion) to the magnetic interaction. The shift of the peak position as R varies from Dy to Tm indicates that the energy scale of the magnetic order decreases relative to the CEF splitting. Such phenomena are consistent with the analysis on the magnetic part of entropy: as shown in the insets of Figs. 16, 18, 20, 22, and 24, Tb, Dy, and Ho compounds manifest fully released S_M at their T_C, whereas Er and Tm compounds still release part of S_M above their T_C, which indicates that unlike R =Gd-Ho members, the CEF splitting for the $4f$ electronic configuration of the Tm^{3+} and Er^{3+} may extend above magnetic ordering temperature.

Based on the assumption that the Fe and Co series have similar CEF splitting (for similar R ions), the comparison between the magnetic ordering temperature and the CEF splitting for different R ions is qualitatively diagrammatized in Fig. 29. The levels represent the single-ion CEF splitting

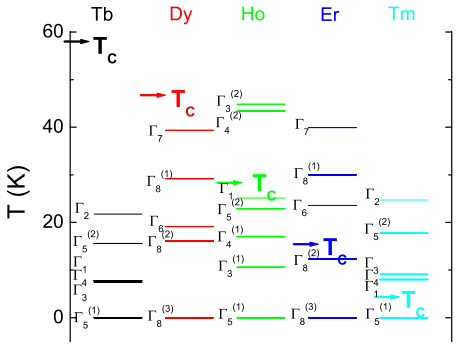

FIG. 29. (Color online) Single-ion CEF splitting energy levels for RCo$_2$Zn$_{20}$ (R=Tb-Tm). The arrows present the T_C values for RFe$_2$Zn$_{20}$ with respective R.

of Hund's ground state of $4f$ electronic configuration of R^{3+}, determined from RCo$_2$Zn$_{20}$, and the arrows represent the T_C values of RFe$_2$Zn$_{20}$. The T_C value is comparable with the highest energy level of CEF splitting for R=Ho. For R=Er and Tm, the T_C values are about $\frac{1}{2}$ and $\frac{1}{5}$ of the highest CEF levels, respectively. This diagram, though it cannot be used to determine the precise energy splitting of the RFe$_2$Zn$_{20}$ compounds (the CEF levels have been strongly modulated and mixed by the interaction energy), is qualitatively consistent with the specific heat measurements and indicates that at least for TmFe$_2$Zn$_{20}$, the CEF energy splitting already happens well above its T_C. In summary, it appears plausible that, due to extremely similar liganal environments, equivalent members of the RFe$_2$Zn$_{20}$ and RCo$_2$Zn$_{20}$ series have similar CEF splitting schemes.

Further insight can also be gained from a careful revisiting of the transport data. The total resistivity of RFe$_2$Zn$_{20}$ (R=Gd-Yb) can be written as

$$\rho(T) = \rho_0 + \rho_{ph}(T) + \rho_{mag}(T), \tag{9}$$

where ρ_{mag} is associated with scattering from the $4f$ moments and the spin fluctuation of itinerant electrons. As seen in Fig. 30(a), for the whole series above 250 K, the resistivity data sets show essentially linear behavior with slopes differing by less than 12% within the estimated dimension error ($\pm 10\%$) of these bar-like-shape samples. These similar high temperature behaviors indicate that, in the high temperature limit, the magnetic scattering is saturated and the phonon scattering is essentially similar for the whole series (due to the very dilute nature of the R ions). Therefore, the magnetic contribution to the resistivity can be estimated by (1) subtracting residue resistivity, ρ_0, (2) normalizing the high temperature slope of all $\rho(T)$ to that of LuFe$_2$Zn$_{20}$, and then (3) subtracting the $\rho_{Lu}(T) - \rho_{Lu0}$ data from the normalized data. The result is written as

$$\Delta\rho(T) = (\rho_R - \rho_{R0}) \frac{\frac{d\rho_R}{dT}\big|_{275\ K}}{\frac{d\rho_{Lu}}{dT}\big|_{275\ K}} - (\rho_{Lu} - \rho_{Lu0}). \tag{10}$$

As shown previously, the subtraction background $\rho_{Lu}(T)$ already includes the scattering associated with the spin fluctuation of itinerant electrons. Thus $\Delta\rho$ will not only include

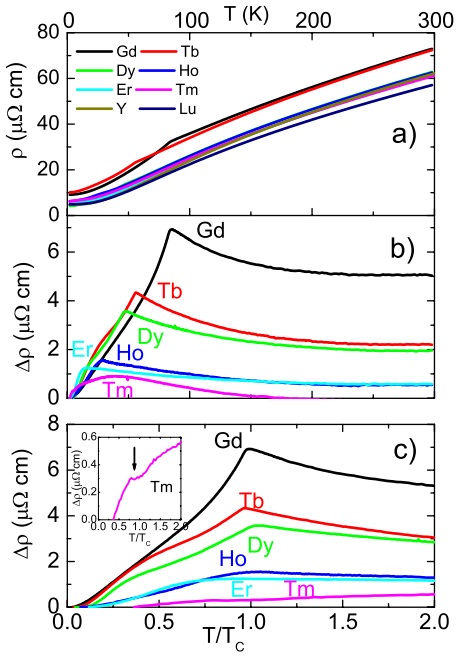

FIG. 30. (Color online) (a) ρ versus T, (b) $\Delta\rho$ versus T, and (c) $\Delta\rho$ versus T/T_C for RFe$_2$Zn$_{20}$ (R=Gd-Tm). Inset: the blow-up $\Delta\rho$ data for TmFe$_2$Zn$_{20}$. The arrow presents the FM ordering temperature.

the scattering from the $4f$ moments but also include scattering associated with the interaction between the $4f$ moments and itinerant electrons. Figures 30(b) and 30(c) show $\Delta\rho$ versus temperature, as well as normalized temperature (T/T_C) for R=Gd-Tm. For R=Gd-Er, a pronounced upward cusp, whose height decreases from Gd to Er, is centered about T_C, whereas TmFe$_2$Zn$_{20}$ manifests a broad feature and only very weak anomaly around its T_C (see the blow-up inset of Fig. 30). As shown in Fig. 27(b), the maximum values of the cusps for different R scale with the de Gennes factor, which indicates that the decrease in $\Delta\rho$ with T below T_C is the result of a loss of spin disorder scattering of conduction electrons, associated with the $4f$ local moment. However, as found in the pseudoternary compounds Gd$_x$Y$_{1-x}$Fe$_2$Zn$_{20}$,[12] the decreasing behavior of $\Delta\rho$ with increasing T above T_C is more conspicuous and must come from a different conduction electron scattering process [simple models of $\rho(T)$ due to magnetic scattering cannot explain this anomaly[35,36]]. Given that RT_2Zn$_{20}$ compounds only manifest this behavior when the local moments are embedded in the highly polarizable background (GdCo$_2$Zn$_{20}$ does not show this behavior[10]), this anomaly is thought to be associated with the spin fluctuation of the $3d$ electrons. Also appearing in the resistivity of RCo$_2$ (R=Gd-Tm),[37] this decreasing behavior of $\Delta\rho$ with increasing T above T_C has been explained as the result of the increase in the spin fluctuation of $3d$ electrons, which is provided by the increasing nonuniform fluctuating $4f$-d electron exchange interaction, as the temperature approaches T_C in the paramagnetic state. Since both Y(Lu)Co$_2$ and Y(Lu)Fe$_2$Zn$_{20}$ are classical examples of NFFLs, such an anomaly could be associated with these strongly correlated electron systems. On the other hand, considering that Hund's ground state of Tm^{3+} has been significantly split above the T_C for TmFe$_2$Zn$_{20}$, it is not unexpected that the conduction electron scattering process manifests a different behavior associated with the CEF effect.

Finally, the nearly FM compounds YFe$_2$Zn$_{20}$ and LuFe$_2$Zn$_{20}$ also merit some further discussion. Shown in Fig. 3, the low field susceptibility (H=10 kOe) manifests a maximum near 6 and 8 K for YFe$_2$Zn$_{20}$ and LuFe$_2$Zn$_{20}$, respectively. Such a maximum in the temperature-dependent susceptibility also appears for other examples of nearly FM compounds. For example, Pd manifests $T_{max} \sim 70$ K,[20] YCo$_2$ and LuCo$_2$ manifests $T_{max} \sim 100$ K,[21] and TiBe$_2$ manifests $T_{max} \sim 10$ K.[22] Another interesting phenomena in nearly FM materials are the so-called itinerant electron metamagnetism (IEM), which is an applied magnetic field induced first-order phase transition between a paramagnetic state and spin polarized state.[38] Experimentally, IEM has been observed for YCo$_2$ and LuCo$_2$ around 70 T.[39,40] Within the framework of Landau theory, the maximum in temperature-dependent susceptibility is thought to be related to IEM.[41] The magnetic part of the free energy ΔF can be written as the function of the magnetic moment M,

$$\Delta F = \tfrac{1}{2}aM^2 + \tfrac{1}{4}bM^4 + \tfrac{1}{6}cM^6, \tag{11}$$

where a, b, and c are the Landau expansion coefficients.

As shown by Shimizu,[41] the condition for the existence of IEM is $a>0$, $b<0$, $c>0$, and $3/16<ac/b^2<9/20$. Within the framework of the spin fluctuation theory, Yamada[42] generalized this work by introducing a temperature-dependent function of the mean square amplitude of spin fluctuations. These theoretical works demonstrated that the existence of IEM is associated with the maximum in $\chi(T)$ by means of the factor of ac/b^2, which can be estimated as

$$\frac{ac}{b^2} = \left[1 - \frac{\chi(0)}{\chi(T_{max})}\right]^{-1}. \tag{12}$$

Furthermore, the IEM can only happen below T_{max}. These results seem to be consistent with the experimental results in various itinerant electronic systems.[43]

According to Eq. (12), the values of ac/b^2 can be estimated as 310 and 72 for YFe$_2$Zn$_{20}$ and LuFe$_2$Zn$_{20}$, respectively [$M/H \sim \chi(T)$ at 10 kOe], which are much larger than the region of the existence of IEM, indicating that IEM may not exist. Indeed, recent measurements on a part of the LuFe$_2$Zn$_{20}$ sample used for the magnetization data in Fig. 3 in a pulse magnetic field up to 55 T at 0.3 K show no evidence of metamagnetic transition. In nearly FM materials, no evidence of IEM appears for TiBe$_2$,[44] which also manifests a relatively low value of T_{max}. From these points of view, Y(Lu)Fe$_2$Zn$_{20}$ and TiBe$_2$ may represent the examples of NFFLs different from YCo$_2$ and LuCo$_2$.

This lack of an IEM sheds further light on the magnetic properties of the local moment bearing RFe$_2$Zn$_{20}$ (R=Gd-Tm) compounds. As shown before, all the members

manifest second-order paramagnetic to ferromagnetic phase transitions. This behavior is different from that seen in the RCo$_2$ (R=Gd-Tm) system: the magnetic phase transitions of R=Dy-Tm members for RCo$_2$ are first order whereas R =Gd and Tb members have second-order transitions.[5] This difference is not difficult to explain in Landau theory: unlike Y(Lu)Co$_2$, the host of Y(Lu)Fe$_2$Zn$_{20}$ lacks of ability to show IEM and therefore cannot be induced to show metamagnetic transition by any molecular field associated with the 4f local moments.

V. SUMMARY

RFe$_2$Zn$_{20}$ and RCo$_2$Zn$_{20}$ (R=Gd-Lu, Y) demonstrate diverse magnetic properties. The conspicuous differences between these two related series are mainly associated with the conduction electron polarizability of the host (nonmagnetic) compounds. YFe$_2$Zn$_{20}$ and LuFe$_2$Zn$_{20}$ manifest similar nearly ferromagnetic properties. When 4f local moments are embedded in this highly polarizable medium, the RFe$_2$Zn$_{20}$ (R=Gd-Tm) series shows highly enhanced FM ordering temperatures. In contrast, YCo$_2$Zn$_{20}$ and LuCo$_2$Zn$_{20}$ manifest normal Pauli paramagnetic behaviors. In a related manner, GdCo$_2$Zn$_{20}$ and TbCo$_2$Zn$_{20}$ show low temperature AFM ordering, and the magnetic properties for RCo$_2$Zn$_{20}$ (R =Dy-Tm) are more strongly influenced by the CEF splitting of the R ions (the dominant energy scale). The CEF coefficients determined for the Co series are consistent with the observed anisotropies of the Fe series, indicating that the CEF splitting of the R ions is similar for the all Zn Frank-Kasper polyhedra that fully encompass the R site. On the other hand, YbFe$_2$Zn$_{20}$ and YbCo$_2$Zn$_{20}$ manifest different heavy Fermion behaviors.

ACKNOWLEDGMENTS

The authors thank J. Frederich for growing some of the compounds, L. Tan for Laue x-ray measurements, and E. D. Mun, Y. Janssen, and R. Prozorov for helpful discussions. Ames Laboratory is operated for the U.S. Department of Energy by Iowa State University under Contract No. DE-AC02-07CH11358. This work was supported by the Director for Energy Research, Office of Basic Energy Sciences.

APPENDIX A

Figure 31 shows the magnetization (at H=1000 Oe) and zero applied field resistivity for three batches of TbFe$_2$Zn$_{20}$, which were synthesized from different initial molar ratios of starting elements, Tb:Fe:Zn=2:3:95, 2:4:94, and 2:5:93. The T_C (determined as 52 ± 2, 56 ± 1, and 67 ± 2 K by resistivity measurements for the three samples) increases as the initial concentration of Fe in the solution increases. We also found similar features for R=Gd and Er, but the variation in their T_C values is less than in the Tb case (Fig. 32). Comparative single-crystal x-ray diffraction measurements performed on the samples, albeit inconclusive, indicated that the crystallographic differences were perhaps due to subtle variations in occupancy of the Fe site.[18] The main difficulty

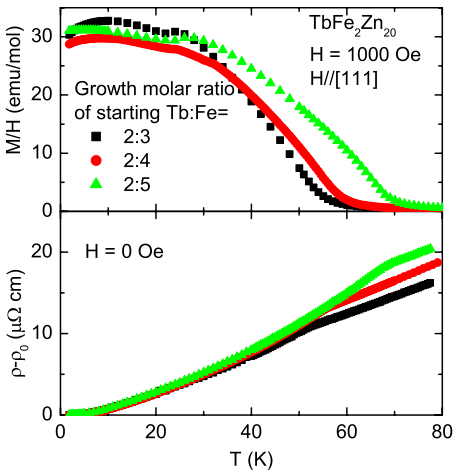

FIG. 31. (Color online) (a) Temperature-dependent M/H for TbFe$_2$Zn$_{20}$(H=1000 Oe) from different initial growth molar ratio of starting elements; (b) temperature-dependent ρ in zero applied field.

associated with the x-ray diffraction measurement was completely resolving the mixed site occupancies for Zn and Fe which have similar atomic number values. Recently, carefully prepared pieces of TbFe$_2$Zn$_{20}$ samples with the same geometric dimensions, from the starting elements, Tb:Fe:Zn=2:3:95 and 2:5:93, were measured using single-crystal neutron diffraction.[19] This measurement showed that the Fe site has ~1% deficiency for the 2:3:95 sample. All these crystallographic measurements indicate the sensitivity of the magnetic properties to the small disorder for RFe$_2$Zn$_{20}$ in this family which has local moments submerged in a highly polarizable conduction electron matrix.

APPENDIX B

As shown in Fig. 1, the distance between the rare-earth ion and the Zn NNs, as well as NNNs, is close to 3 Å, whereas the distance with the next nearest neighbors (six Zn in 48f site) is larger than 5 Å. Due to this isolated cagelike configuration of rare-earth ions, the effect of ions other than this CN-16 Frank-Kasper polyhedron can be neglected in the

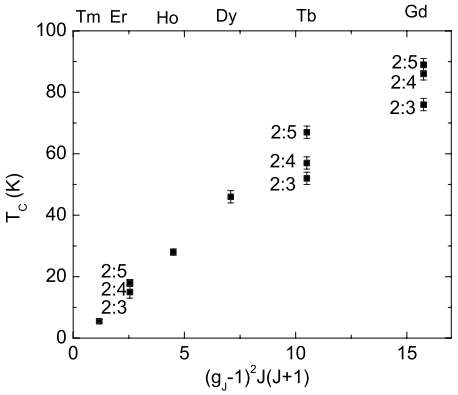

FIG. 32. T_C values for different growth of RFe$_2$Zn$_{20}$ (R =Gd-Tm) samples with respect to the de Gennes factor.

calculation of the CEF coefficients based on the point charge model.

Appreciably, the ligands of the rare-earth ions in the C-15 Laves compounds ($R\mathrm{Ni}_2$) form a same polyhedron, whose CEF coefficients have been calculated by Bleaney[45] based on the point charge model. Therefore, one can directly cite the following results:

$$B_4^0 = -\frac{3}{2}\left(\frac{91e^2Z_1}{726R_1^5} - \frac{7e^2Z_2}{54R_2^5}\right)\langle r^4\rangle\langle J\|\beta\|J\rangle, \tag{B1}$$

$$B_6^0 = \frac{9}{16}\left(-\frac{8e^2Z_1}{363R_1^7} - \frac{8e^2Z_2}{81R_2^7}\right)\langle r^6\rangle\langle J\|\gamma\|J\rangle, \tag{B2}$$

where Z_1e and Z_2e are the charges of the NN and NNN ions ($Z_1=Z_2=2$ for Zn^{2+}), R_1 and R_2 is the distance between the R ion and the two sets of ions, $\langle r^4\rangle$ and $\langle r^6\rangle$ are the mean fourth and sixth powers of the electronic radius for the $4f$ electrons, and β and γ are the Steven multiplicative factors. Extracting the values of $\langle r^4\rangle$ and $\langle r^6\rangle$ from Ref. 46, β and γ values from Ref. 31, and R_1 and R_2 values from the results of single-crystal x-ray diffraction,[18] one can calculate the B_4^0 and B_6^0 values (shown in Table II).

*Present address: Department of Chemistry, Princeton University, Princeton, NJ 08544.

[1] J. J. M. Franse and R. J. Radwanski, in *Handbook of Magnetic Materials*, edited by K. H. J. Buschow (Elsevier, Amsterdam, 1993), Vol. 7, pp. 307–501.

[2] A. Szytula and J. Leciejewicz, *Handbook of Crystal Structures and Magnetic Properties of Rare Earth Intermetallics* (CRC Press, Cleveland, 1994).

[3] T. Moriya, *Spin Fluctuations in Itinerant Electron Magnetism* (Springer-Verlag, Berlin, 1985).

[4] N. H. Duc and T. Goto, in *Handbook on the Physics and Chemistry of Rare Earths*, edited by K. A. Gschneidner, Jr. and L. Eyring (Elsevier, Amsterdam, 1999), Vol. 26, pp. 177–264.

[5] N. H. Duc and P. E. Brommer, in *Handbook of Magnetic Materials*, edited by K. H. J. Buschow (Elsevier, Amsterdam, 1999), Vol. 12, pp. 259–394.

[6] T. Nasch, W. Jeitschko, and U. C. Rodewald, Z. Naturforsch., B: Chem. Sci. **52**, 1023 (1997).

[7] P. I. Kripyakevich and O. S. Zarechnyuk, Dopov. Akad. Nauk Ukr. RSR, Ser. A: Fiz.-Tekh. Mat. Nauki **30**, 364 (1968).

[8] V. M. T. Thiede, W. Jeitschko, S. Niemann, and T. Ebel, J. Alloys Compd. **267**, 23 (1998).

[9] O. Moze, L. D. Tung, J. J. M. Franse, and K. H. J. Buschow, J. Alloys Compd. **268**, 39 (1998).

[10] S. Jia, S. L. Bud'ko, G. D. Samolyuk, and P. C. Canfield, Nat. Phys. **3**, 334 (2007).

[11] M. S. Torikachvili, S. Jia, E. D. Mun, S. T. Hannahs, R. C. Black, W. K. Neils, D. Martien, S. L. Bud'ko, and P. C. Canfield, Proc. Natl. Acad. Sci. U.S.A. **104**, 9960 (2007).

[12] S. Jia, N. Ni, S. L. Bud'ko, and P. C. Canfield, Phys. Rev. B **76**, 184410 (2007).

[13] S. Jia, N. Ni, G. D. Samolyuk, A. Safa-Sefat, K. Dennis, H. Ko, G. J. Miller, S. L. Bud'ko, and P. C. Canfield, Phys. Rev. B **77**, 104408 (2008).

[14] P. C. Canfield and Z. Fisk, Philos. Mag. B **65**, 1117 (1992).

[15] R. D. Shannon, Acta Crystallogr., Sect. A: Cryst. Phys., Diffr., Theor. Gen. Crystallogr. **32**, 751 (1976).

[16] E. M. Benbow and S. E. Latturner, J. Solid State Chem. **179**, 3989 (2006).

[17] P. Villars and L. D. Calvert, *Pearson's Handbook of Crystallographic Data for Intermetallic Phases* (ASM, International Materials Park, OH, 1996).

[18] Hyunjin Ko, A. Safa-Sefat, Shuang Jia, S. L. Bud'ko, P. C. Canfield, and G. J. Miller (unpublished).

[19] A. D. Christianson *et al.* (unpublished).

[20] W. Gerhardt, F. Razavi, J. S. Schilling, D. Hüser, and J. A. Mydosh, Phys. Rev. B **24**, 6744 (1981).

[21] E. Burzo, E. Gratz, and V. Pop, J. Magn. Magn. Mater. **123**, 159 (1993).

[22] W. Gerhardt, J. S. Schilling, H. Olijnyk, and J. L. Smith, Phys. Rev. B **28**, 5814 (1983).

[23] A. P. B. Zellermann and J. Voitländer, J. Phys.: Condens. Matter **16**, 919 (2004).

[24] P. Larson, I. I. Mazin, and D. J. Singh, Phys. Rev. B **69**, 064429 (2004).

[25] M. Shimizu, J. Phys. Soc. Jpn. **16**, 1114 (1961).

[26] F. Acker, Z. Fisk, J. L. Smith, and C. Y. Huang, J. Magn. Magn. Mater. **22**, 250 (1981).

[27] T. Jeong, A. Kyker, and W. E. Pickett, Phys. Rev. B **73**, 115106 (2006).

[28] χ and γ values of Pd and YCo_2 are extracted from G. S. Knapp and R. W. Jones, Phys. Rev. B **6**, 1761 (1972); K. Ikeda, K. A. Gschneidner, R. J. Stierman, T.-W. E. Tsang, and O. D. McMasters, Phys. Rev. B **29**, 5039 (1984).

[29] K. D. Myers, S. L. Bud'ko, I. R. Fisher, Z. Islam, H. Kleinke, A. H. Lacerda, and P. C. Canfield, J. Magn. Magn. Mater. **205**, 27 (1999).

[30] K. W. H. Stevens, Proc. Phys. Soc., London, Sect. A **65**, 209 (1952).

[31] K. R. Lea, M. J. M. Leask, and W. P. Wolf, J. Phys. Chem. Solids **23**, 1381 (1962).

[32] J. M. Fournier and E. Gratz, in *Handbook on the Physics and Chemistry of Rare Earths*, edited by K. A. Gschneidner, Jr., L. Eyring, G. H. Lander, and G. R. Choppin (North-Holland, Amsterdam, 1993), Vol. 17, pp. 409–537.

[33] K. U. Neumann and K. R. A. Ziebeck, J. Magn. Magn. Mater. **140-144**, 967 (1995).

[34] J. Pierre, in *Magnetism of Metals and Alloys*, edited by M. Cyrot (North-Holland, Amsterdam, 1982), pp. 245–293.

[35] P. P. Craig, W. I. Goldburg, T. A. Kitchens, and J. I. Budnick, Phys. Rev. Lett. **19**, 1334 (1967).

[36] M. E. Fisher and J. S. Langer, Phys. Rev. Lett. **20**, 665 (1968).

[37] E. Gratz, R. Resel, A. T. Burkov, E. Bauer, A. S. Markosyan, and A. Galatanu, J. Phys.: Condens. Matter **7**, 6687 (1995).

[38] E. P. Wohlfarth and P. Rhodes, Philos. Mag. **7**, 1817 (1962).

[39] T. Goto, K. Fukamichi, T. Sakakibara, and H. Komatsu, Solid

State Commun. **72**, 945 (1989).
[40] T. Goto, T. Sakakibara, K. Murata, H. Komatsu, and K. Fukamichi, J. Magn. Magn. Mater. **90&91**, 700 (1990).
[41] M. Shimizu, J. Phys. (Paris) **43**, 155 (1981).
[42] H. Yamada, Phys. Rev. B **47**, 11211 (1993).
[43] T. Goto, K. Fukamichi, and H. Yamada, Physica B **300**, 167 (2001).
[44] H. Yamada and K. Terao, Physica B **246&247**, 502 (1998).
[45] B. Bleaney, Proc. R. Soc. London, Ser. A **276**, 28 (1963).
[46] A. J. Freeman and R. E. Watson, Phys. Rev. **127**, 2058 (1962).